Charge exchange in collisions of 1-100-keV Sn3+ ions with H2 and D2

Rai, S.; Bijlsma, K. I.; Rabadán, I.; Méndez, L.; Wolff, P. A.J.; Salverda, M.; Versolato, O. O.; Hoekstra, R.

Published in:
Physical Review A

DOI:
10.1103/PhysRevA.106.012804

Charge exchange in collisions of 1–100-keV Sn^{3+} ions with H_2 and D_2

S. Rai [1,2] K. I. Bijlsma [1,2] I. Rabadán [3] L. Méndez [3] P. A. J. Wolff [1] M. Salverda [1]
O. O. Versolato [2,4] and R. Hoekstra [1,2,*]

[1]*Zernike Institute for Advanced Materials, University of Groningen, Nijenborgh 4, 9747 AG Groningen, The Netherlands*
[2]*Advanced Research Center for Nanolithography (ARCNL), Science Park 106, 1098 XG Amsterdam, The Netherlands*
[3]*Laboratorio Asociado al CIEMAT de Física Atómica y Molecular en Plasmas de Fusión, Departamento de Química, Universidad Autónoma de Madrid, Cantoblanco E-28049 Madrid, Spain*
[4]*Department of Physics and Astronomy and LaserLab, Vrije Universiteit Amsterdam, De Boelelaan 1081, 1081 HV Amsterdam, The Netherlands*

(Received 14 February 2022; accepted 15 June 2022; published 11 July 2022)

Absolute cross sections for single electron capture by Sn^{3+} colliding with H_2 and D_2 have been measured and calculated in the energy range of 1–100 keV. The cross sections are determined by measuring the change in ion beam current with varying target density and by measuring the yields of charged target fragments by means of a time-of-flight spectrometer. The results for D_2 show good agreement with our seven-state semiclassical calculations, while for H_2 the experimental results increase more strongly than the calculations toward lower energies. This discrepancy is attributed to vibrational effects, not included in the calculations, that lead to the breakdown of the Franck-Condon approximation.

DOI: 10.1103/PhysRevA.106.012804

I. INTRODUCTION

Charge exchange in collisions of keV-energy multiply charged ions with neutral species remains an active research topic ever since the advent of highly charged ion sources (e.g., Refs. [1–3]). Experiments have continually challenged, in ever-increasing detail, the theoretical approaches, which were initially classical and subsequently semiclassical in their description of the electron dynamics during the interactions (e.g., Ref. [4]). The bulk of the research has dealt with low-Z ions, because the number of active electrons and quantum states to be included in the calculations is limited and because intense ion beams can most easily be produced from low-Z, gaseous species. More complex and heavier ions, in particular intermediately charged Fe ions, have been studied (e.g., Refs. [5–7]) because of their astrophysical and fusion plasma relevance. Over the past years, Sn ions have moved into the focus of highly charged ion physics [8–14] as Sn alloys are considered for fusion plasma vapor shielding [15–17] and because laser-produced Sn plasma is the source of 13.5-nm extreme ultraviolet (EUV) light driving state-of-the-art EUV nanolithography machines [18–22]. In such machines, multilayer mirror optics collect and guide the EUV light [23,24]. To prevent damage to the optics by the energetic Sn ions [25–27], the plasma is embedded in H_2 gas. Fundamental data on charge exchange and stopping in $Sn^{q+} + H_2$ collisions is missing though it is crucial for accurate and predictive modeling.

Here in a joint experimental and theoretical study, absolute cross sections for single electron capture (SC) from H_2 (and its heavier isotopologue D_2) by Sn^{3+}, i.e., for the reaction

$$Sn^{3+} + H_2 \rightarrow Sn^{2+} + H_2^+ \tag{1}$$

are determined. The choice for starting out with Sn^{3+} ions is based on its alkali-like electronic configuration: $[Kr]5d^{10}5s$. For alkali-like ion beams, metastable fractions are negligible [28], making the collision systems tractable to experiment and theory. In the experiments, Sn^{3+} ions in the energy range of 9 to 51 keV are used as projectiles. Due to the high mass of the Sn ions, this corresponds to low velocities of 0.05 to 0.13 a.u. The cross section measurements are based on the measurement of the changes in ion beam current with changing target density. Therefore, in the determination of the SC cross sections one needs to consider possible contributions of two-electron processes: bound double capture [BDC, Eq. (2a)] and autoionizing double capture [ADC, Eq. (2b)].

$$Sn^{3+} + H_2 \rightarrow Sn^{+} + 2H^{+}, \tag{2a}$$

$$Sn^{3+} + H_2 \rightarrow Sn^{2+} + 2H^{+} + e. \tag{2b}$$

BDC is expected to have a small cross section because the two-electron capture channel closest to resonance is the one leading to capture into the $[Kr]\ 5d^{10}\ 5s^2\ 5p$ ground electronic configuration of Sn^+ which is endothermic by approximately 6 eV. All other $5s^2\ nl$ configurations are more endothermic and thus not likely to be populated at all. ADC requires population of doubly excited levels of even much higher endothermicity. Therefore, it is safe to exclude ADC from our analysis. The BDC contribution is extracted from time-of-flight (ToF) spectrometry on the target fragments. In BDC, the two protons resulting from the Coulomb explosion of $[H_2]^{2+}$ get kinetic

*Corresponding author: r.a.hoekstra@rug.nl

energies of 9.7 eV each, while in SC reactions the few protons created next to the by far dominant H_2^+ production channel have energy close to 0 eV. The yield of 9.7-eV protons is used to correct the data for any BDC contribution. At the same time, this allows for an assessment of the BDC cross sections.

The calculations of SC total cross sections for ion-molecule collisions are carried out by applying methods based on those developed for ion-atom collisions; for instance, at the energies of the present work, expansions in terms of electronic functions of the quasimolecule formed during the collision, within either semiclassical or quantal frameworks. Besides the obvious difference of treating a many-center system, there are two important characteristics of ion-molecule collisions that must be taken into account. First, in the semiclassical treatment, where the projectile follows a classical trajectory, the probabilities of a given process depend on the orientation of the molecule with respect to the ion trajectory. It is necessary to average the calculated cross sections over a set of collisions with different molecular orientations. The methodology employed in this work (Ref. [29] and references therein) employs molecular data (electronic energies and dynamical couplings) calculated along the trajectory. The second important difference of ion-molecule collisions with respect to ion-atom collisions is the presence of molecular nuclear motion. The use of vibronic bases to simultaneously describe the electronic and vibrational motions leads to cumbersome calculations, however, that allowed us to reproduce the maximum of the electron capture cross section found in detailed experiments for H^+–H_2 collisions, and explain this maximum as a consequence of the interplay between electronic and nuclear motions [30].

In the following section, Sec. II A describes the experimental setup, while Secs. II B–II E present the actual measurement procedure and all the calibration and data analysis steps. Section III describes the theoretical approaches used to calculate single-electron capture in collisions of Sn^{3+} on either H_2 or D_2. Thereafter, the experimental and theoretical data are compared and discussed in Sec. IV.

II. EXPERIMENTAL METHODS

The data presented in this work have been obtained by colliding a beam of monoenergetic Sn^{3+} ions with a neutral gas target (H_2 or D_2) in a series of crossed-beam type of experiments. The ions are extracted from an Electron Cyclotron Resonance Ion Source (ECRIS) stationed at the ZERNIKE Low Energy Ion-Beam Facility (ZERNIKELEIF) at the University of Groningen. Ions with energies in the range of $3q$ to $25q$ keV can be generated, where q is the charge state of the ion. The ions extracted from the ion source are selected for a given mass-over-charge ratio (m/q) using a 110° analyzing magnet with a resolution of about 0.5%. ^{120}Sn is the most abundant isotope of Sn but for a charge state of 3, the corresponding m/q is 40 which is the same as that of Ar^+. Hence, to prevent possible contamination of the Sn^{3+} beam by Ar^+ impurities, $^{118}Sn^{3+}$ is used. Sn atoms are introduced into the source chamber by heating a crucible oven filled with solid tin. The analyzed ion beam is transported through the central beamline and steered into the gas target setup by a 45° bending magnet.

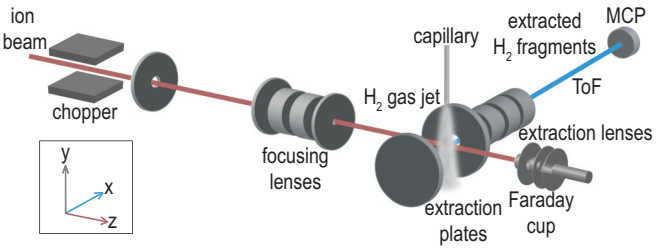

FIG. 1. Schematic of the crossed-beam setup, CHEOPS, used to measure charge exchange cross section for keV Sn^{3+} ions colliding on H_2 (and D_2).

A. The crossed-beam setup

The relevant features of the gas target setup, CHEOPS (charge exchange observed by particle spectroscopy) are depicted in Fig. 1. The ion beam is collimated by a set of four apertures, the smallest one of 1 mm diameter, positioned at the entrance of the collision chamber. In the chamber, the base pressure is $\approx 2\times10^{-8}$ mbar. A ϕ 0.5-mm grounded capillary is located 14 mm above the center of the ion beam. The gas flowing into the chamber, via the capillary, is regulated by a high-precision mass flow controller (Bronkhorst FG-200CV), thus creating a localized jet of H_2 target gas, which is crossed by the beam. A flow rate of 1 ml/min was used throughout the experiments unless stated otherwise and the corresponding chamber pressure for that flow is $\approx 1.5\times10^{-4}$ mbar. The ions are collected at the end of the setup by a Faraday cup (FC) and the beam current is measured using a Keithley 6485 picoammeter. The FC assembly consists of three components: (i) the entrance cap with a ϕ 3-mm aperture, (ii) a ϕ 6-mm guard ring, and (iii) the FC. The guard ring is biased at −38 V to suppress the escape of secondary electrons from the FC. The cap shields the collision chamber from the field of the guard ring. The whole FC assembly is mounted on an XY translation stage. By scanning the assembly in the horizontal and vertical plane and recording the current at the cap and FC, a typical beam width of ≈1.5 mm at the FC is determined.

Charged collision fragments produced in the central crossed-beam region can be extracted towards a time-of-flight (ToF) spectrometer, which allows for measuring the yields of atomic H^+ and molecular H_2^+ ions. The ToF measurements (see Sec. II D) require the continuous ion beam to be chopped in short pulses to have a start pulse for the spectrometer. At a rate of up to 8 kHz, short ≈20 ns ion beam pulses are generated by sweeping the ion beam over the entrance aperture by means of alternating the opposite voltages on two electrodes (chopper plates; see Fig. 1).

Fragments under the influence of the field across the collision center pass through a ϕ 5-mm aperture into the ToF spectrometer. An electrostatic lens system consisting of four elements is then used to accelerate and focus the fragments into the ToF tube floating at −1700 V. Toward the end of the tube, the fragments get detected by a microchannel plate (MCP) detector whose front plate is set to −2100 V. The total flight length from the collision center to the detector is 1.13 m. The MCP detector is connected to a pick-off amplifier followed by a constant-fraction discriminator (CFD) to amplify and filter the signals. The output of the discriminator is fed

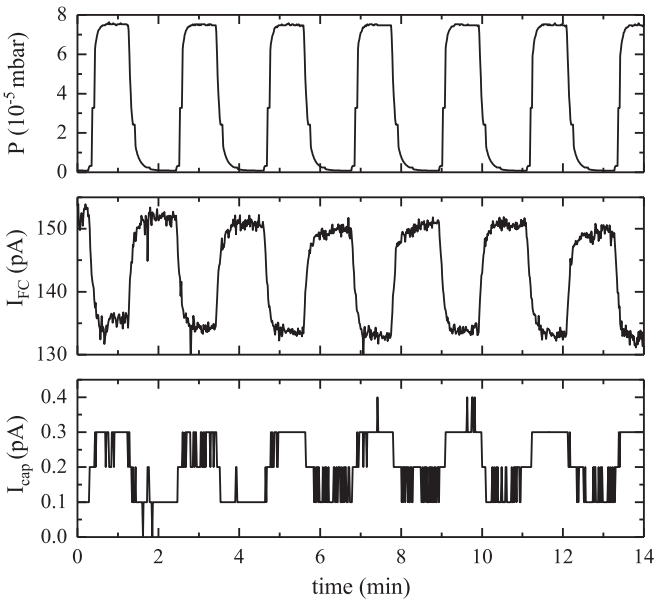

FIG. 2. Typical time trace: Variation of ion beam current measured at the Faraday cup (middle panel) and the cap (lower panel) with toggling H_2 flow rate between 0 and 0.5 ml/min. The top panel shows the associated time trace of the pressure in the collision chamber.

to a multihit time-to-digital converter (TDC, FAST P7888) in order to record the ToF spectrum.

B. Procedure of measuring charge exchange cross sections

Figure 2 shows the time trace of a typical measurement run. The flow controller is programmed to sequentially start and stop the flow of gas into the chamber. The top panel in the figure shows the variation of chamber pressure with acquisition time. When the gas flows from the capillary into the chamber, the ion beam crossing the gas may undergo charge exchange collisions. This leads to a decrease in the beam current measured by the FC as shown in the middle panel of the figure. The collision of the ions with the gas also results in angular scattering of the ion beam. If the scattered ions hit the cap, current is generated and recorded as depicted in the bottom panel of the figure. The effect is small, however; the change in cap current is typically around 1% of the change in FC current.

The full set of differential equations describing the evolution of the charge state of the ions along their trajectory (z) through the collision chamber is as follows:

$$\frac{dN^{3+}}{dz} = -(\sigma_{32}+\sigma_{31})nN^{3+}, \tag{3a}$$

$$\frac{dN^{2+}}{dz} = \sigma_{32}nN^{3+} - (\sigma_{21}+\sigma_{20})nN^{2+}, \tag{3b}$$

$$\frac{dN^{1+}}{dz} = \sigma_{31}nN^{3+} + \sigma_{21}nN^{2+} - \sigma_{10}nN^{1+}, \tag{3c}$$

$$\frac{dN^{0+}}{dz} = \sigma_{20}nN^{2+} + \sigma_{10}nN^{1+}. \tag{3d}$$

In the low-density, single-collision regime the set of equations is reduced to

$$\frac{dN^{3+}}{dz} = -(\sigma_{32}+\sigma_{31})nN^{3+}. \tag{4}$$

Here, σ_{ij} denotes the cross section for electron capture by an ion in an initial charge state i leading to a final charge state j, n is the number density of the target, and N^{q+} denotes the number of Sn ions with charge state q. The numbers of ions are related to the ion current I measured in the FC via $I = qN^{q+} + (q-1)N^{(q-1)+} + (q-2)N^{(q-2)+}$. The differential equation for single-collision conditions, Eq. (4), can be solved analytically, yielding the following general relation between ion beam current and the single-capture cross section σ_{SC} (or $\sigma_{q,q-1}$)

$$\sigma_{SC} = \frac{-\ln\left(a\frac{I}{I_o} - b\right)}{(1+f)\int_0^L n(z)dz}, \tag{5}$$

where I_0 is the initial ion current, f is the ratio between two- and one-electron capture ($f = \frac{\sigma_{BDC}}{\sigma_{SC}}$), $a = \frac{(1+f)q}{1+2f}$, $b = \frac{(1+f)q-(1+2f)}{1+2f}$, and L is the path length the ions travel through the collision chamber. Here for Sn^{3+}, $q = 3$. As will be discussed in detail in Sec. II D, the bound double capture fraction f is estimated experimentally from ToF measurements on target fragments (H^+ and H_2^+). However, first in Sec. II C the determination of the integral target density $\int_0^L n(x)dx$ is presented.

C. Calibration of the integral target density

Accurate, absolute target density measurements over the ion trajectory are difficult. Therefore, we determine the integral target density using a reference collision system for which the charge exchange cross sections are very well known: $H^+ + H_2$; see, e.g., the data review by Nakai *et al.* [32]. From the review paper, we see that for protons only single electron capture (σ_{10}) needs to be considered; in the energy range of 5 to 20 keV, double electron capture is approximately two orders of magnitude smaller than one-electron capture [32]. This implies that Eq. (5) for protons on H_2 simplifies significantly (with $f = 0$ and $q = 1$) and can be rewritten to

$$\int_0^L n(z)dz = -\frac{\ln\frac{I}{I_o}}{\sigma_{10}} = \beta P \tag{6}$$

to extract the integral target density from a measurement of the change of proton current. Here β is introduced as the proportionality factor between the integral target density and the pressure P in the collision chamber. From the many studies reported in Nakai's review paper [32], we used the cross sections σ_{10} reported by McClure [31] for calibration. McClure's set of cross sections covers our range of interest, and at energies of 5 keV and lower, there is excellent agreement with the results of an elaborate joint experimental and theoretical study by Urbain *et al.* [30].

Figure 3 shows σ_{10} cross sections for $H^+ + H_2$. The dashed curve shows a trend line through the reference data of McClure [31] and the associated gray band depicts the systematic ±5% uncertainty on the McClure data. The solid squares represent our measurements, which were fitted to the reference line with a single common factor. In this way, for the

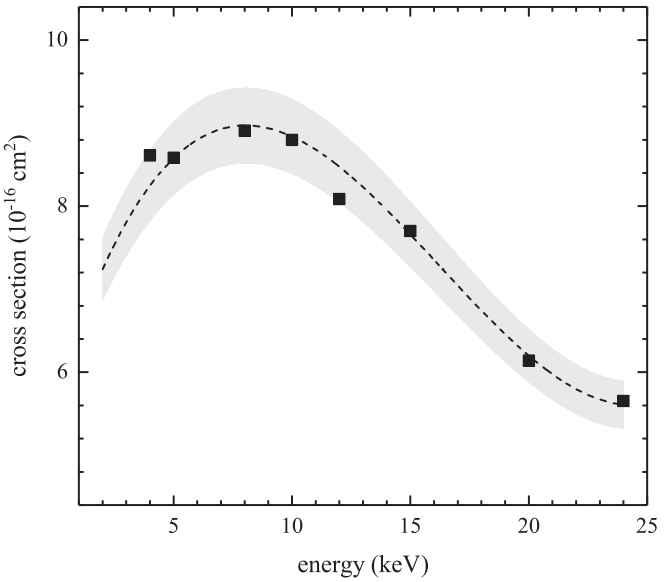

FIG. 3. Single-electron capture cross section for protons on H_2 (solid squares). Dashed curve: trend line through reference data [31]. The gray band depicts the ±5% systematic uncertainty associated with the McClure data.

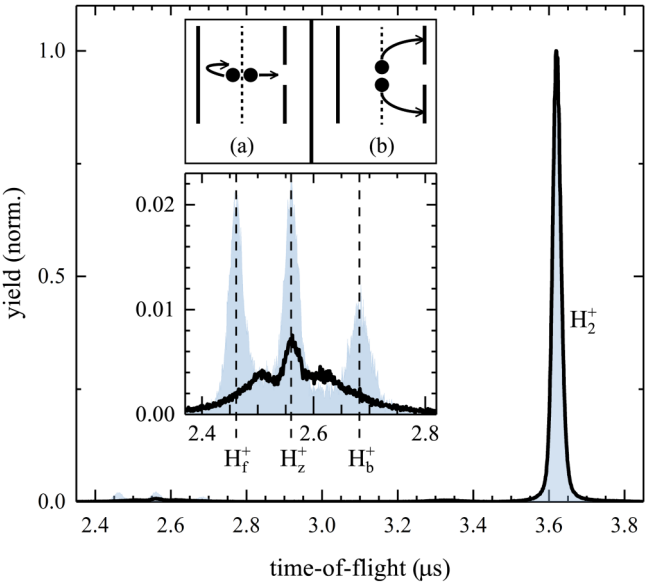

FIG. 4. Time-of-flight (ToF) spectra of target fragments for 48 keV Sn^{3+} (line) and 50 keV N^{5+} (fill) colliding on H_2. For direct comparison, the spectra are normalized to the H_2^+ peak height. The enlargement shows the very weak proton peaks. Expected peak positions for 9.7-eV protons from BDC are marked by dashed lines. H_f^+ and H_b^+ refer to forward and backward emitted protons respectively. The position of 0-eV protons, H_z^+, of course lying between H_f^+ and H_b^+, is also marked by a dashed line for reference.

scaling factor β a value of 1.03 ($\pm$ 0.07)$\times 10^{18}$ cm^{-2} mbar^{-1} is determined.

The integral target density changes with the choice of gas. Therefore, we also measure β for D_2, the other target gas used in the experiments, and find a value of 1.15 ($\pm$ 0.08) $\times 10^{18}$ cm^{-2} mbar^{-1}. Here it is assumed that the cross sections for H_2 and D_2 are the same as their ionization potentials are equal and the proton velocities are rather high (0.4–1 a.u.) [33,34].

D. Determination of two-electron capture contributions to the CX measurements

From Eq. (5) it is seen that one needs to know f, the ratio between BDC and SC, to obtain the SC cross sections. The distribution of target fragments allows for the assessment of the ratio between BDC and SC. SC [Eq. (1)] generates molecular ions H_2^+ of ≈0 eV. The capture of two electrons [Eqs. (2b), (2a)] leads to dissociation of the H_2 molecule into two energetic protons of 9.7 eV. Figure 4 shows two typical ToF spectra, one for Sn^{3+} and one for N^{5+} colliding on H_2. In both cases, the strongest peak is the H_2^+ peak associated with SC [cf. Eq. (1)]. The contribution of protons to the ToF spectrum is weak.

As can be seen in the zoom in Fig. 4, the proton "peak" consists of three peaks of which the central one is located at the expected ToF of H^+ fragments and represents protons of ≈0 eV stemming from gentle dissociation of H_2^+ molecular ions excited just above the dissociation limit (see, e.g., Ref. [35]). The two peaks on either side of the 0-eV proton peak correspond to 9.7-eV protons from BDC where the peak at slightly shorter ToFs belongs to 9.7-eV protons emitted in the forward direction to the ToF spectrometer (H_f^+) and the one at longer ToFs is due to protons emitted backward, away from the ToF spectrometer (H_b^+). Backward emitted protons get reflected by the extraction field [see Fig. 4(a)] into the direction of the ToF spectrometer, explaining the time difference between the forward and backward emitted 9.7-eV protons. The difference in ToF (ΔT) scales with the square root of the kinetic energy release (U_{KER}) of the dissociation process (e.g., Ref. [36]) and for singly charged fragments it is given by

$$\Delta T = \frac{\sqrt{8\,\mu\,U_{\mathrm{KER}}}}{E}, \tag{7}$$

with E being the extraction field (in the present experiment 40 V/cm) with the reduced mass, μ, being 0.5 and 1 for H_2 and D_2 respectively.

The 9.7-eV protons emitted along the beam axis are intercepted by the entrance diaphragm of the ToF spectrometer; see Fig. 4(b). Therefore, in general, only 9.7-eV protons emitted in small cones towards or away from the ToF spectrometer are detected, leading to the two proton peaks labeled H_f^+ and H_b^+ in Fig. 4, respectively. Using 50-keV N^{5+} and 60-keV O^{6+} ions colliding with H_2 as reference systems for which cross sections for single-electron capture and for bound and autoionizing double-electron capture have been measured [37–43], the percentage of the 9.7-eV protons that is detected in our experimental setup, α, is determined to be (5 ± 1)%.

Figure 4 compares the ToF spectra, normalized to their H_2^+ peak heights, of 48-keV Sn^{3+} and 50-keV N^{5+} colliding with H_2^+. While the 9.7-eV H_f^+ and H_b^+ are very prominent for N^{5+} they are barely present for Sn^{3+}. This hints at a significantly lower double capture contribution in the case of Sn^{3+} ions than for N^{5+} for which single and double capture are of

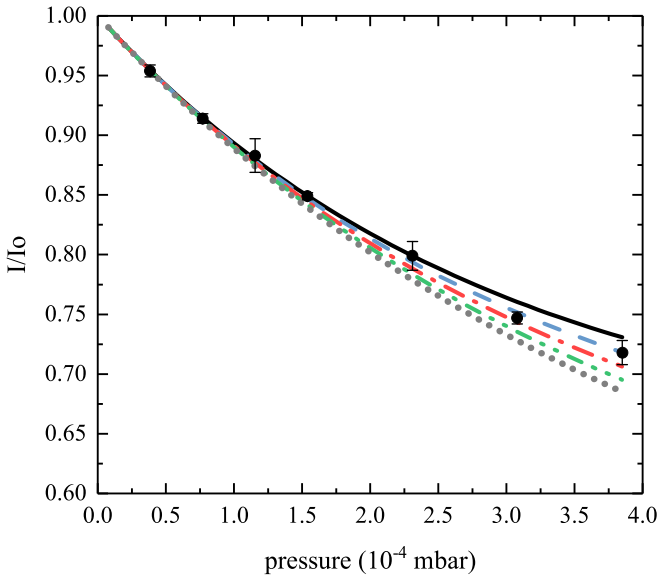

FIG. 5. Comparison of the measured beam current of 39-keV Sn^{3+} ions (black symbols) as a function of the H_2 target pressure with simulated results (solid curves) taking different values for the σ_{21} cross section ($Sn^{2+} \rightarrow Sn^{1+}$). For σ_{21}, the following cross sections are used (in units of 10^{-16} cm^2) for the lines of different colors and styles: black, 0; blue dashed, 2.5; red dash dotted, 5; green dash dot dotted, 7.5; and gray dotted, 10.

similar magnitude. Over the energy range of 10–50 keV, the ratio f of double-over-single capture for Sn^{3+} is determined to be $(11 \pm 4)\%$. The uncertainty in f is quite considerable due to the low intensities of the 9.7-eV H_f^+ and H_b^+ peaks. Peak areas for H_f^+ and H_b^+ are assessed by fitting Gaussian peaks to the spectrum while applying the following constraints: (i) the positions and separation (223 ns) between the 9.7-eV H_f^+ and H_b^+ peaks are fixed; (ii) the ratio of the 9.7-eV H_f^+ and H_b^+ peak areas is set to 1.3; and (iii) the width of the H_f^+ peak is fixed at 1.5 times the width of the H_b^+ peak. The fitting constraints for the 9.7-eV H_f^+ and H_b^+ peaks, which were determined on basis of the N^{5+} and O^{6+} spectra, were also observed in numerous ToF measurements with other ions, e.g., Xe^{4+}, Sn^{5+}, and Ar^{6+}.

E. Contributions of double collisions

Finally, it is checked that the experiments are performed in the single-collision regime by varying the target pressure over one order of magnitude. Figure 5 shows as an example the dependence of the measured beam current of Sn^{3+} as a function of target pressure. In the figure, the solid curves are generated by solving Eqs. (3) taking only the significant cross sections namely σ_{32}, σ_{31}, and σ_{21}. The measured σ_{32} and f are used as inputs in the calculations; the multiple curves correspond to calculations taking different input values of σ_{21}. From the figure, it is seen that deviations from the single-collision approximation might start to show up at pressures of 1.5×10^{-4} mbar depending on the magnitude of the cross section for single-electron capture (σ_{21}) by Sn^{2+}. The data in Fig. 5 suggest a σ_{21} cross section of about 5×10^{-16} cm^2. As the data used for the final determination of the single-electron cross sections σ_{32} have been taken at 1.5×10^{-4} mbar, the influence of double collisions is very small and might have been neglected. Nevertheless, we have chosen to correct the data for double collisions assuming a common σ_{21} cross section of $(5 \pm 5)\times10^{-16}$ cm^2. Such inclusion of double collisions reduces the uncorrected σ_{32} cross sections by ≈3% on average.

III. THEORY

We have calculated the SC cross sections using a semiclassical method with nuclear straight-line trajectories. The calculation assumes that the H–H internuclear distance, ρ, is fixed during the collision (Franck-Condon approximation). The electronic wave function has been expanded in terms of seven molecular functions of the SnH_2^{3+} quasimolecule. The molecular wave functions are approximate eigenfunctions of the Born-Oppenheimer electronic Hamiltonian, obtained by means of a multireference configuration interaction method. In practice, the calculation explicitly considers the three valence electrons, which move in the field created by the H nuclei and the *ab initio* pseudopotential STUTTGART RLC ECP [44] that describes the electrons' interaction with the Sn^{4+} core. We have carried out the calculation of electronic wave functions by employing a three-center basis set of Gaussian-type-orbitals (GTO) that includes the $(8s, 4p) \rightarrow [3s, 2p]$ basis [45] centered on the H nuclei and a $[4s, 4p, 3d, 2f]$ basis [46] on the Sn nucleus. In a first step, we have obtained a set of molecular orbitals (MOs) in a restricted Hartree-Fock calculation in this basis for the SnH_2^{3+} system, and we have created the configuration space by allowing single and double excitations from a set of eight reference configurations. The configuration space is restricted by allowing between one and three electrons in five MOs, the first four orbitals of A′ symmetry and the first A″ MO. Up to two electrons can occupy the remaining orbitals. We have calculated the nonadiabatic couplings numerically as explained in Refs. [47,48] with a differentiation step of 10^{-4} a.u. The molecular expansion includes a common translation factor based on the switching function of Ref. [49].

The asymptotic energy differences between the entrance channel $Sn^{3+}(5s^1\,{}^2S) + H_2(X\,{}^1\Sigma_g^+)$ and the exit channels $Sn^{2+}(5s^2\,{}^1S, 5s5p\,{}^3P^o, 5s5p\,{}^1P^o, 5p^2\,{}^3P)$ have been compared with NIST data [50], after subtracting the calculated ionization potential of H_2 at the equilibrium distance ($\rho = 1.4$ a.u.). The differences with the average energies of each multiplet are smaller than 0.03 a.u.. In Fig. 6, we show the energies of the seven lowest molecular states for a nuclear geometry with the angle between the vectors $\boldsymbol{R}$ ($\boldsymbol{R}$ is the position vector of the Sn nucleus with respect to the midpoint of the H-H internuclear axis) and $\boldsymbol{\rho}$ equal to 60°, which has been found in previous calculations [51] to be a representative geometry that leads to cross sections in good agreement with the orientation-averaged (OA) ones. In the nonrelativistic approach, only transitions to doublet states are allowed. Also, transitions to A'' are forbidden, and we have plotted only the energies of the molecular states $^2A'$. The energy of the entrance channel exhibits avoided crossings with those of the states dissociating into $Sn^{2+}(5s5p\,{}^1P^o)+H_2^+(X\,{}^2\Sigma_g^+)$ and

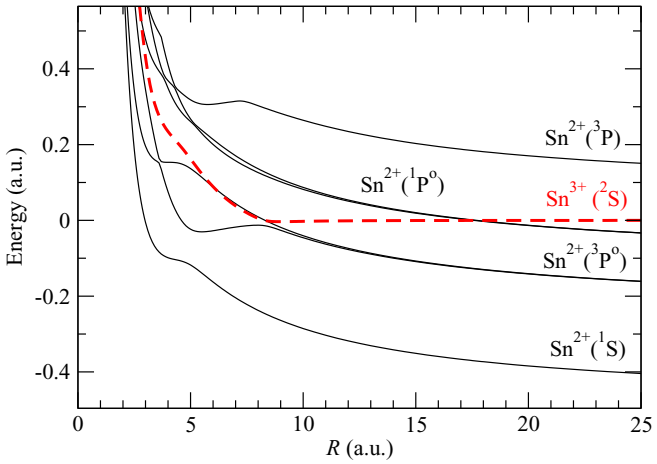

FIG. 6. Potential energy curves of the $(Sn+H_2)^{3+}\ ^2A'$ electronic states as functions of the distance from the Sn nucleus to the midpoint of the H_2 axis. The spectroscopic terms of the Sn^{2+} or Sn^{3+} ions in the separate atom limit are indicated in the figure.

$Sn^{2+}(5s5p\,^3P^o)+H_2^+(X\,^2\Sigma_g^+)$. The first one takes place at a very large distance, $R \approx 17.5$ a.u., and is very narrow. In practice, it is traversed diabatically, as plotted in Fig. 6. At not too high collision energies, the transitions in the neighborhood of the second avoided crossing, $R \approx 8.5$ a.u., furnish the main mechanism of the electron capture process. As the collision energy increases, the transitions in the wide avoided crossing between the energies of the ground and the first excited state at $R \approx 5$ a.u., become more important, and are responsible for the population of the channel $Sn^{2+}(5s^2\,^1S)+H_2^+(X\,^2\Sigma_g^+)$.

The numerical solution of the eikonal equation leads to the probabilities for transitions to the different capture channels, $P_k(b)$ and the corresponding integral cross sections,

$$\sigma_k = 2\pi \int_0^\infty bP_k(b)db, \tag{8}$$

where b is the impact parameter.

In Fig. 7, we plot the opacity functions, bP_k, for the electron capture into $Sn^{2+}(^1S)+H_2^+(X^2\Sigma_g^+)$, $Sn^{2+}(^3P^o)+H_2^+(X^2\Sigma_g^+)$ and $Sn^{2+}(^1P^o)+H_2^+(X^2\Sigma_g^+)$ for the collision energies of 250 eV/u and 500 eV/u. One can note that the charge transfer channel, $Sn^{2+}(^3P^o)+H_2^+(X^2\Sigma_g^+)$, is populated for relatively large impact parameters, which are coherent with the predicted transitions in the avoided crossing at $R \approx 8.5$ a.u.. At these energies, the transitions near the avoided crossing between the two first energy curves give rise to the observed transitions at $b \lesssim 5.5$ a.u. to the electronic state dissociating in $Sn^{2+}(^1S)+H_2^+(X^2\Sigma_g^+)$, which are more important as E decreases. On the contrary, the probabilities for capture to $Sn^{2+}(^3P^o)+H_2^+(X^2\Sigma_g^+)$ are less important as E increases, which corresponds to a more diabatic crossing of the avoided crossing near $R \approx 8.5$ a.u..

A more elaborate treatment of the orientation average is provided by the trajectory average where the energies and couplings are calculated along the projectile trajectory (see Ref. [29]). In the present case, we have carried out cross section calculations with three trajectory orientations as explained in Ref. [52].

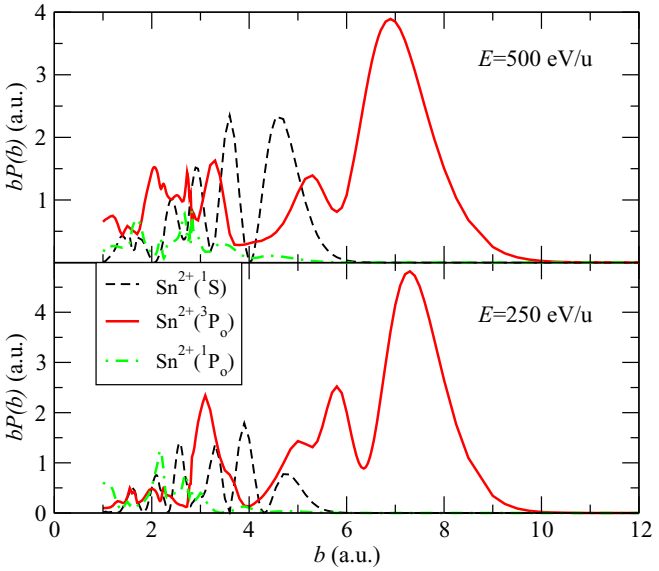

FIG. 7. Opacity functions for the main three CX channels at $E = 250$ eV/u (bottom) and $E = 500$ eV/u (top).

IV. RESULTS AND DISCUSSION

The experimental results for Sn^{3+} colliding with H_2 are presented in Fig. 8 (solid black dots). The measured cross sections range between $(25–50)\times10^{-16}$ cm^2 and increase in magnitude with decreasing ion energy. For instance, on moving down from 0.43 to 0.08 keV/u in ion energy, the cross sections increase by a factor of ≈2. The cross sections are compared to our semiclassical calculations shown by the full black curve labeled OA in Fig. 8. The experiments and the theory agree fairly well at higher energies but as one moves toward lower impact energies, a discrepancy emerges. In the

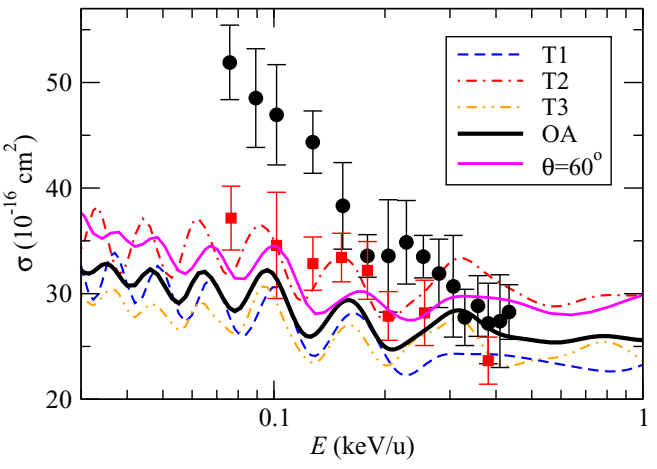

FIG. 8. Comparison of experimental data with different semiclassical calculations of single electron capture cross sections in Sn^{3+} collision with H_2 (black circles) and D_2 (red squares) as functions of the ion energy. The semiclassical results for the seven molecular states are obtained along three trajectory orientations (T1, T2, and T3) and their average (OA). The result of an isotropic calculation with the energies and couplings calculated for a fixed angle, 60°, between $\boldsymbol{v}$ and $\boldsymbol{\rho}$ is also included.

case of the calculated cross sections, the increase toward lower energy is much weaker with the cross section increasing by only a factor of ≈1.2 on going down from 0.43 to 0.08 keV/u in impact energy. In search of the prospective cause of this discrepancy, experiments with the heavier isotopologue D_2 have been conducted, the results of which are given by the red solid squares in Fig. 8. A remarkable isotope effect is observed in the experiments. Also, the calculations, which are independent of the molecular mass, evidently show better agreement (even at lower energies) with the experiments performed with D_2.

At relatively high impact energies, the main difficulty of the semiclassical calculation comes from the need to perform calculations for different orientations of the molecule with respect to the projectile trajectory or, equivalently, for different trajectory orientations with respect to a fixed molecule. We show in Fig. 8 the cross sections calculated for three trajectory orientations (T1, T2, and T3), where T1 is a trajectory with $\boldsymbol{v} \parallel \boldsymbol{\rho}$ and $\boldsymbol{b} \perp \boldsymbol{\rho}$, T2 with $\boldsymbol{v} \perp \boldsymbol{\rho}$ and $\boldsymbol{b} \parallel \boldsymbol{\rho}$, and T3 with $\boldsymbol{v} \perp \boldsymbol{\rho}$ and $\boldsymbol{b} \perp \boldsymbol{\rho}$, with [52]

$$\sigma_{OA} = \tfrac{1}{3}[\sigma(\mathrm{T1}) + \sigma(\mathrm{T2}) + \sigma(\mathrm{T3})]. \tag{9}$$

In this system, the orientation effects are expected to be small because the main transitions take place at large internuclear separations. This is confirmed by the small differences between the three orientation-dependent results, and also between the OA cross section and that obtained using the energies and couplings calculated for $\theta = 60^\circ$ (≈ 6%). It can be noted in this figure that the oscillatory behavior of the cross section is similar in all calculations. The origin of these oscillations can be traced back to the interferences between transitions in the avoided crossing at $R \approx 8.5$ a.u. and those at $R \approx 3.6$ a.u. (see Fig. 6), which also appear in the calculations along the trajectories T1–T3. Since the transitions take place at relatively large values of R, the oscillations are similar and they do not disappear in the OA cross section.

The seven-state molecular calculation has been carried out within the framework of the semiclassical method, which may limit the validity of the calculation at relatively low collision energies. To estimate the limitation of this approximation, we have carried out exploratory full quantal calculations with a basis set of two molecular states, those involved in the avoided crossing at $R \approx 8.5$ a.u.: $Sn^{3+}(^2S)+H_2$ and $Sn^{2+}(^3P^o)+H_2^+(^2\Sigma_g^+)$. The semiclassical and the quantal two-state calculations show good agreement in the energy region 20 eV/u $< E <$ 100 eV/u (Fig. 9), which indicates that the differences found with the experimental values are not due to the use of the semiclassical formalism. In this respect, one must note that in the semiclassical method, the two molecular states are coupled by the two components of the nuclear gradient in the collision plane. However, in the quantal formalism (see Ref. [30]), only the component in the radial direction is included. In Fig. 9, we have plotted the semiclassical cross section calculated without the coupling that comes from the gradient component perpendicular to the radial direction, which is identical to the quantal one. Therefore, trajectory and quantal effects can be neglected in the energy range of the experiment.

A second approximation of the semiclassical calculation is the neglect of the spin-orbit coupling. An estimate of the influence of this effect is obtained in both the quantal and the multichannel Landau-Zener (MCLZ) calculations with the Hamiltonian matrix elements given by the formulas of Ref. [53] and adding the asymptotic splitting of the $Sn^{2+}(^3P^o)$ term [50] to the diagonal matrix elements. The ensuing cross section has similar values to the experimental ones for $E > 0.2$ keV/u, but it decreases at lower energies. To further check this model, we have carried out a similar estimate by performing a four-state quantal calculation with the numerical H data previously employed in the two-state calculation and adding the asymptotic L-S splitting at all ion-molecule separations. At low energies, the cross section is dominated by transitions at large R to the highest state with $J = 2$ and it is increased with respect to that from the two-state calculation by up to 10%, because the avoided crossing is moved to a larger R as a consequence of the energy shift. For $E > 500$ eV/u (not shown in Fig. 9), the model cross section shows an increase that is due to transitions to the lowest level ($J = 0$) that take place at smaller R, where the approximation of keeping the two-state interaction is not valid. We have also carried out a numerical experiment by integrating numerically the matrix elements of Ref. [53] with the asymptotic splitting, as in the MCLZ estimate. For the sake of clarity, the results are not included in Fig. 9; they are similar to those using the numerical data, but without the oscillations, because the matrix elements of Ref. [53] do not include the modeling of the inner avoided crossing.

Finally, the increasing difference between the experimental cross sections for collisions with H_2 and D_2, as energy decreases, can be due to vibrational effects. In this respect, a similar isotopic dependency was found in the experiment of Kusakabe *et al.* [33] for H^++(H_2, D_2). It is expected that the Franck-Condon calculation shows better agreement with D_2 data than with H_2 because it assumes that the target

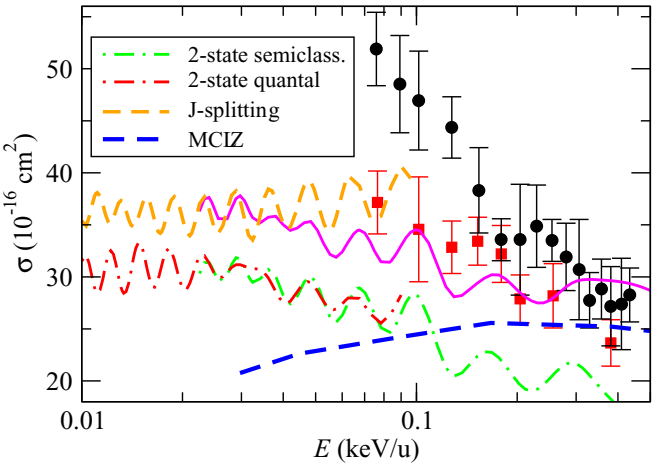

FIG. 9. Comparison of the isotropic seven-state semiclassical calculation with $\theta = 60^\circ$ (solid pink line) with a two-state quantal calculation and a two-state semiclassical calculation without rotational couplings (dash-dotted lines). The dashed lines are the estimates including the effect of the L-S coupling (labeled J splitting) in a four-state quantal calculation and in the multichannel Landau-Zener (MCLZ) model. The experimental results are also included as in Fig. 8.

bond length remains fixed during the collision and this is a more realistic description for D_2 than for H_2, given that the larger reduced mass of the first is linked to a more localized initial vibrational wave function. Nevertheless, as the collision energy decreases, the vibrational effects will also start to be relevant for D_2 and we expect that the OA Franck-Condon calculation will not be valid for D_2 at energies below the experimental ones. Calculations of charge transfer beyond the Franck-Condon approximation [34] for H^++(H_2, D_2) found good agreement with experiments for both isotopic targets.

V. CONCLUSION

In this work, we have presented both an experimental determination and a theoretical calculation of the absolute single electron capture cross section for Sn^{3+} on H_2 in the energy range 1–100 keV. The experiments are based on measuring a reduction in ion beam current due to the charge exchange interaction. The calculations are done in a semiclassical way using molecular orbitals. At the higher energies, there is a fair agreement between the experimentally determined and the theoretically calculated values. However, the experimental cross sections show a considerable increase toward lower energies, whereas this effect is only weakly present in the calculated values. Exploratory full quantal calculations have been performed and these show good agreement with the semiclassical calculations. From this, we conclude that the discrepancy is not due to the invalidity of the semiclassical approach in our energy regime. The effect of spin-orbit coupling has been found to be small (≈15%) and it does not explain the rise of the cross section for the collision with H_2 at $E < 200$ eV/u. The experiments have also been performed for the heavier isotopologue D_2 and show a less strong increase of cross section toward the lower energies and are in good agreement with the semiclassical Franck-Condon calculations. This leads us to conclude that the increase for H_2 is due to vibrations in the target molecule. This effect is weaker in D_2 because of the higher mass and it is not included in the calculations, which make use of the Franck-Condon approximation.

ACKNOWLEDGMENTS

The experimental work was carried out at the ZERNIKELEIF facility in the Zernike Institute for Advanced Materials of the University of Groningen as part of the research portfolio of the Advanced Research Center for Nanolithography, a public-private partnership between the University of Amsterdam, the Vrije Universiteit Amsterdam, the Dutch Research Council (NWO), and the semiconductor equipment manufacturer ASML. The theoretical work of I.R. and L.M. was partially supported by Ministerio de Economía, Industria y Competitividad (Spain), Project No. FIS2017-84684-R. The computational support by the Centro de Computación Científica of UAM is also acknowledged.

[1] R. Geller, Electron cyclotron resonance sources: Historical review and future prospects, Rev. Sci. Instrum. **69**, 1302 (1998).

[2] R. K. Janev and H. Winter, State-selective electron capture in atom-highly charged ion collisions, Phys. Rep. **117**, 265 (1985).

[3] M. Barat and P. Roncin, Multiple electron capture by highly charged ions at keV energies, J. Phys. B: At. Mol. Opt. Phys. **25**, 2205 (1992).

[4] W. Fritsch and C. D. Lin, The semiclassical close-coupling description of atomic collisions: Recent developments and results, Phys. Rep. **202**, 1 (1991).

[5] I. Čadež, J. B. Greenwood, J. Lozano, R. J. Mawhorter, M. Niimura, S. J. Smith, and A. Chutjian, Absolute cross sections for single and double charge-exchange in Fe^{q+} impacting on He, J. Phys. B: At. Mol. Opt. Phys. **36**, 3303 (2003).

[6] J. Simcic, D. R. Schultz, R. J. Mawhorter, I. Čadež, J. B. Greenwood, A. Chutjian, C. M. Lisse, and S. J. Smith, Measurement and calculation of absolute single- and multiple-charge-exchange cross sections for Fe^{q+} ions impacting CO and CO_2, Phys. Rev. A **81**, 062715 (2010).

[7] I. Y. Tolstikhina, M. S. Litsarev, D. Kato, M.-Y. Song, J.-S. Yoon, and V. P. Shevelko, Collisions of Be, Fe, Mo and W atoms and ions with hydrogen isotopes: Electron capture and electron loss cross sections, J. Phys. B: At. Mol. Opt. Phys. **47**, 035206 (2014).

[8] V. I. Azarov and Y. N. Joshi, Analysis of the $4d^7$-$4d^6 5p$ transition array of the eighth spectrum of tin: Sn VIII, J. Phys. B: At. Mol. Opt. Phys. **26**, 3495 (1993).

[9] R. D'Arcy, H. Ohashi, S. Suda, H. Tanuma, S. Fujioka, H. Nishimura, K. Nishihara, C. Suzuki, T. Kato, F. Koike, J. White, and G. O'Sullivan, Transitions and the effects of configuration interaction in the spectra of Sn XV–Sn XVIII, Phys. Rev. A **79**, 042509 (2009).

[10] A. Windberger, F. Torretti, A. Borschevsky, A. Ryabtsev, S. Dobrodey, H. Bekker, E. Eliav, U. Kaldor, W. Ubachs, R. Hoekstra, J. R. Crespo López-Urrutia, and O. O. Versolato, Analysis of the fine structure of Sn^{11+}-Sn^{14+} ions by optical spectroscopy in an electron-beam ion trap, Phys. Rev. A **94**, 012506 (2016).

[11] F. Torretti, A. Windberger, A. Ryabtsev, S. Dobrodey, H. Bekker, W. Ubachs, R. Hoekstra, E. V. Kahl, J. C. Berengut, J. R. Crespo López-Urrutia, and O. O. Versolato, Optical spectroscopy of complex open-4*d*-shell ions Sn^{7+}-Sn^{10+}, Phys. Rev. A **95**, 042503 (2017).

[12] J. Scheers, C. Shah, A. Ryabtsev, H. Bekker, F. Torretti, J. Sheil, D. A. Czapski, J. C. Berengut, W. Ubachs, J. R. Crespo López-Urrutia, R. Hoekstra, and O. O. Versolato, EUV spectroscopy of highly charged Sn^{13+}-Sn^{15+} ions in an electron-beam ion trap, Phys. Rev. A **101**, 062511 (2020).

[13] N. R. Badnell, A. Foster, D. C. Griffin, D. Kilbane, M. O'Mullane, and H. P. Summers, Dielectronic recombination of heavy species: The tin $4p^6 4d^q$-$4p^6 4d^{(q-1)} 4f + 4p^5 4d^{(q+1)}$ transition arrays for $q = 1$–10, J. Phys. B: At. Mol. Opt. Phys. **44**, 135201 (2011).

[14] A. Borovik, Jr, M. F. Gharaibeh, P. M. Hillenbrand, S. Schippers, and A. Müller, Detailed investigation of electron-impact single-ionization cross sections and plasma rate coefficients of *N*-shell tin ions, J. Phys. B: At. Mol. Opt. Phys. **46**, 175201 (2013).

[15] G. G. van Eden, T. W. Morgan, D. U. B. Aussems, M. A. van den Berg, K. Bystrov, and M. C. M. van de Sanden, Self-Regulated Plasma Heat Flux Mitigation Due to Liquid Sn Vapor Shielding, Phys. Rev. Lett. **116**, 135002 (2016).

[16] R. E. Nygren and F. L. Tabarés, Liquid surfaces for fusion plasma facing components: A critical review. Part I: Physics and PSI, Nucl. Mater. Energy **9**, 6 (2016).

[17] G. G. van Eden, V. Kvon, M. C. M. van de Sanden, and T. W. Morgan, Oscillatory vapour shielding of liquid metal walls in nuclear fusion devices, Nat. Commun. **8**, 192 (2017).

[18] G. O'Sullivan, B. Li, R. D'Arcy, P. Dunne, P. Hayden, D. Kilbane, T. McCormack, H. Ohashi, F. O'Reilly, P. Sheridan, E. Sokell, C. Suzuki, and T. Higashiguchi, Spectroscopy of highly charged ions and its relevance to EUV and soft x-ray source development, J. Phys. B: At. Mol. Opt. Phys. **48**, 144025 (2015).

[19] W. Svendsen and G. O'Sullivan, Statistics and characteristics of XUV transition arrays from laser-produced plasmas of the elements tin through iodine, Phys. Rev. A **50**, 3710 (1994).

[20] V. Bakshi, editor, *EUV Lithography*, 2nd ed. (SPIE, Bellingham, WA, 2018).

[21] O. O. Versolato, Physics of laser-driven tin plasma sources of EUV radiation for nanolithography, Plasma Sources Sci. Technol. **28**, 083001 (2019).

[22] V. Y. Banine, K. N. Koshelev, and G. H. P. M. Swinkels, Physical processes in EUV sources for microlithography, J. Phys. D: Appl. Phys. **44**, 253001 (2011).

[23] I. Fomenkov, D. Brandt, A. Ershov, A. Schafgans, Y. Tao, G. Vaschenko, S. Rokitski, M. Kats, M. Vargas, M. Purvis, R. Rafac, B. La Fontaine, S. De Dea, A. LaForge, J. Stewart, S. Chang, M. Graham, D. Riggs, T. Taylor, M. Abraham *et al.*, Light sources for high-volume manufacturing EUV lithography: Technology, performance, and power scaling, Adv. Opt. Techn. **6**, 173 (2017).

[24] F. Torretti, J. Sheil, R. Schupp, M. M. Basko, M. Bayraktar, R. A. Meijer, S. Witte, W. Ubachs, R. Hoekstra, O. O. Versolato, A. J. Neukirch, and J. Colgan, Prominent radiative contributions from multiply-excited states in laser-produced tin plasma for nanolithography, Nat. Commun. **11**, 2334 (2020).

[25] A. Bayerle, M. J. Deuzeman, S. van der Heijden, D. Kurilovich, T. de Faria Pinto, A. Stodolna, S. Witte, K. S. E. Eikema, W. Ubachs, R. Hoekstra, and O. O. Versolato, Sn ion energy distributions of ns- and ps-laser produced plasmas, Plasma Sources Sci. Technol. **27**, 045001 (2018).

[26] D. J. Hemminga, L. Poirier, M. M. Basko, R. Hoekstra, W. Ubachs, O. O. Versolato, and J. Sheil, High-energy ions from Nd:YAG laser ablation of tin microdroplets: Comparison between experiment and a single-fluid hydrodynamic model, Plasma Sources Sci. Technol. **30**, 105006 (2021).

[27] L. Poirier, A. Bayerle, A. Lassise, F. Torretti, R. Schupp, L. Behnke, Y. Mostafa, W. Ubachs, O. O. Versolato, and R. Hoekstra, Cross-calibration of a combined electrostatic and time-of-flight analyzer for energy-and charge-state-resolved spectrometry of tin laser-produced plasma, Appl. Phys. B **128**, 39 (2022).

[28] R. F. Welton, T. F. Moran, and E. W. Thomas, Metastable state abundances in multiply charged ion beams, J. Phys. B: At. Mol. Opt. Phys. **24**, 3815 (1991).

[29] I. Rabadán and L. Méndez, Orientation effects in ion-molecule collisions, J. Phys.: Conf. Ser. **875**, 012009 (2017).

[30] X. Urbain, N. de Ruette, V. M. Andrianarijaona, M. F. Martin, L. Fernández Menchero, L. F. Errea, L. Méndez, I. Rabadán, and B. Pons, New Light Shed on Charge Transfer in Fundamental $H^+ + H_2$ Collisions, Phys. Rev. Lett. **111**, 203201 (2013).

[31] G. W. McClure, Electron transfer in proton-hydrogen-atom collisions: 2–117 keV, Phys. Rev. **148**, 47 (1966).

[32] Y. Nakai, T. Shirai, T. Tabata, and R. Ito, Cross sections for charge transfer of hydrogen atoms and ions colliding with gaseous atoms and molecules, At. Data Nucl. Data Tables **37**, 69 (1987).

[33] T. Kusakabe, L. Pichl, R. J. Buenker, M. Kimura, and H. Tawara, Isotope effect in charge-transfer collisions of slow H^+ and D^+ ions with H_2, HD, and D_2 molecules, Phys. Rev. A **70**, 052710 (2004).

[34] L. F. Errea, L. Fernández, L. Méndez, B. Pons, I. Rabadán, and A. Riera, Vibronic treatment of vibrational excitation and electron capture in $H^+ + H_2$ (HD, D_2,...) collisions at low impact energies, Phys. Rev. A **75**, 032703 (2007).

[35] S. Martínez, G. Bernardi, P. Focke, A. D. González, and S. Suárez, H_2 dissociation by H^+ and He^{2+} projectiles at intermediate energies, J. Phys. B: At. Mol. Opt. Phys. **36**, 4813 (2003).

[36] H. O. Folkerts, F. W. Bliek, M. C. de Jong, R. Hoekstra, and R. Morgenstern, Dissociation of CO induced by ions: I. Fragmentation and kinetic energy release spectra, J. Phys. B: At. Mol. Opt. Phys. **30**, 5833 (1997).

[37] D. H. Crandall, M. L. Mallory, and D. C. Kocher, Charge exchange between multicharged ions of C, N, and O and molecular hydrogen, Phys. Rev. A **15**, 61 (1977).

[38] D. Dijkkamp, D. Ciric, E. Vileg, A. de Boer, and F. J. de Heer, Subshell-selective electron capture in collisions of C^{4+}, N^{5+}, O^{6+} with H, H_2 and He, J. Phys. B: At. Mol. Phys. **18**, 4763 (1985).

[39] M. Mack and A. Niehaus, Radiative and Auger decay channels in k-shell excited Li-like ions ($Z = 68$), Nucl. Instrum. Methods Phys. Res. Sect. B **23**, 109 (1987).

[40] M. Mack, Electron spectroscopy in collisions with multiply charged ions, Nucl. Instrum. Methods Phys. Res. Sect. B **23**, 74 (1987).

[41] R. A. Phaneuf, I. Alvarez, F. W. Meyer, and D. H. Crandall, Electron capture in low-energy collisions of C^{q+} and O^{q+} with H and H_2, Phys. Rev. A **26**, 1892 (1982).

[42] G. Lubinski, Z. Juhász, R. Morgenstern, and R. Hoekstra, State-selective electron-capture cross section measurements for low-energy collisions of He-like ions on H_2, J. Phys. B: At. Mol. Opt. Phys. **33**, 5275 (2000).

[43] J. R. Machacek, D. P. Mahapatra, D. R. Schultz, Y. Ralchenko, A. Chutjian, J. Simcic, and R. J. Mawhorter, Measurement and calculation of absolute single- and double-charge-exchange cross sections for O^{6+} ions at 1.17 and 2.33 keV/u impacting He and H_2, Phys. Rev. A **90**, 052708 (2014).

[44] A. Bergner, M. Dolg, W. Küchle, H. Stoll, and H. Preuß, *Ab initio* energy-adjusted pseudo potentials for elements of groups 1317, Mol. Phys. **80**, 1431 (1993).

[45] P.-O. Widmark, P.-Å. Malmqvist, and B. O. Roos, Density matrix averaged atomic natural orbital (ANO) basis sets for correlated molecular wave functions, Theor. Chim. Acta **77**, 291 (1990).

[46] J. M. L. Martin and A. Sundermann, Correlation consistent valence basis sets for use with the Stuttgart-Dresden-Bonn

relativistic effective core potentials: The atoms GaKr and InXe, J. Chem. Phys. **114**, 3408 (2001).

[47] J. F. Castillo, L. F. Errea, A. Macías, L. Méndez, and A. Riera, *Ab initio* calculation of nonadiabatic couplings using MELD, J. Chem. Phys. **103**, 2113 (1995).

[48] L. F. Errea, L. Fernández, A. Macías, L. Méndez, I. Rabadán, and A. Riera, Sign-consistent dynamical couplings between ab initio three-center wave functions, J. Chem. Phys. **121**, 1663 (2004).

[49] L. F. Errea, L. Méndez, and A. Riera, On the choice of translation factors for approximate molecular wavefunctions, J. Phys. B: At. Mol. Phys. **15**, 101 (1982).

[50] A. Kramida, Y. Ralchenko, J. Reader, and NIST ASD Team, NIST Atomic Spectra Database (ver. 5.3), National Institute of Standards and Technology, Gaithersburg, MD, 2015, http://physics.nist.gov/asd.

[51] L. F. Errea, A. Macías, L. Méndez, I. Rabadán, and A. Riera, Anisotropy effects in H^++H_2 collisions, Int. J. Mol. Sci. **3**, 142 (2002).

[52] L. F. Errea, J. D. Gorfinkiel, A. Macías, L. Méndez, and A. Riera, Implementation of the sudden approximation eikonal method in ion-diatom collisions, J. Phys. B: At. Mol. Opt. Phys. **30**, 3855 (1997).

[53] M. Kimura, T. Iwai, Y. Kaneko, N. Kobayashi, A. Matsumoto, S. Ohtani, K. Okuno, S. Takagi, H. Tawara, and S. Tsurubuchi, Landau-Zener model calculations of one-electron capture from He atoms by highly stripped ions at low energies, J. Phys. Soc. Jpn. **53**, 2224 (1984).